GEOPHYSICS

The equation of motion for supershear frictional rupture fronts

David S. Kammer[1]*†, Ilya Svetlizky[2]†, Gil Cohen[2], Jay Fineberg[2]

The rupture fronts that mediate the onset of frictional sliding may propagate at speeds below the Rayleigh wave speed or may surpass the shear wave speed and approach the longitudinal wave speed. While the conditions for the transition from sub-Rayleigh to supershear propagation have been studied extensively, little is known about what dictates supershear rupture speeds and how the interplay between the stresses that drive propagation and interface properties that resist motion affects them. By combining laboratory experiments and numerical simulations that reflect natural earthquakes, we find that supershear rupture propagation speeds can be predicted and described by a fracture mechanics–based equation of motion. This equation of motion quantitatively predicts rupture speeds, with the velocity selection dictated by the interface properties and stress. Our results reveal a critical rupture length, analogous to Griffith's length for sub-Rayleigh cracks, below which supershear propagation is impossible. Above this critical length, supershear ruptures can exist, once excited, even for extremely low preexisting stress levels. These results significantly improve our fundamental understanding of what governs the speed of supershear earthquakes, with direct and important implications for interpreting their unique supershear seismic radiation patterns.

INTRODUCTION

The onset of frictional sliding occurs through the dynamic propagation of rupture fronts (*1*). Local slip occurs only once these fronts rupture the microcontacts that define the rough contacting surfaces that separate sliding bodies. Propagation speeds of idealized rupture fronts that are driven by singular stresses at their tips are limited by the Rayleigh wave velocity (*2*, *3*). However, when regularization of these singularities is taken into account, theoretical (*4*) and numerical (*5*) work has predicted the existence of supershear cracks, a class of cracks that propagate beyond the shear wave speed and may approach the longitudinal wave speed. While supershear ruptures have since been observed in laboratory friction experiments (*6*–*10*) and inferred in natural earthquakes (*11*–*14*), it is not completely understood what determines their speed. Understanding what determines the speed of supershear earthquakes has important implications, as their propagation speeds strongly influence the structure of their radiated waves. The supershear radiation structure, which is fundamentally different from sub-Rayleigh earthquake radiation (*15*), has important consequences for resulting seismic hazards (*16*).

While the conditions for the transition of ruptures from sub-Rayleigh to supershear regime have been studied extensively (*5*, *17*–*22*), the question of what determines the evolution of supershear rupture speed is still entirely open. In the sub-Rayleigh regime, using the framework of linear elastic fracture mechanics (LEFM), the equation of motion for accelerating ruptures has been constructed via the superposition of solutions for constant-velocity (singular) shear cracks (*23*). This solution has recently been validated experimentally for frictional ruptures (*2*, *3*). In the supershear regime, however, this approach fails (*24*, *25*), as the elastic fields in the crack tip vicinity are coupled to the crack velocity history.

Here, we construct an approximate equation of motion for supershear cracks by using a particular solution given by Broberg (*26*). This equation of motion builds on previous work on energy flux for supershear cracks (*26*–*28*) but provides a direct link between crack length and rupture speed. It therefore enables us to predict supershear crack speeds for various nonuniform systems. We will show that this equation of motion provides a good description of both experiments and numerical observations of frictional supershear ruptures that have been proposed to model natural earthquakes. Our results demonstrate the broad applicability and the scope of these approximate solutions. These results demonstrate how predictions based on fracture mechanics can be successfully extended to the supershear regime.

[1]School of Civil and Environmental Engineering, Cornell University, Ithaca, NY 14850, USA. [2]Racah Institute of Physics, Hebrew University of Jerusalem, Jerusalem 91904, Israel.
*Corresponding author. Email: kammer@cornell.edu
†These authors contributed equally to this work.

RESULTS

Sustained supershear propagation

Our experimental setup consists of two poly(methyl methacrylate) (PMMA) plates of same thickness that are pressed together by an applied normal load (Fig. 1A). We use both dry and boundary-lubricated frictional interfaces (*3*). Shear forces F_S are applied, and slip events are either nucleated spontaneously (*7*) or induced (*3*) by a slight out-of-plane shear perturbation at $x \approx 0$. A high-speed camera at 580,000 frames/s records the dynamic changes of the real contact area $A(x, t)$. Figure 1B shows an example of a frictional rupture event that nucleates at $x \approx 0$, accelerates, and transitions at $x \approx 50$ mm to supershear speeds ($C_f > C_S$), which it maintains until reaching the leading edge.

In addition, the stresses σ_{ij} are calculated from strains measured every 1 μs at multiple locations along (and slightly above) the frictional interface (*2*). Figure 1C shows the variation of the shear stress $\tau = \sigma_{xy} - \sigma^r_{xy}$ (σ^r_{xy} is the residual frictional resistance) and the dynamic stress drop τ_0, as the rupture passes by the strain measurement location. At the interface, we expect the shear stress to increase to the peak shear strength of the frictional interface (see definition of τ_p in Fig. 1C). Although this highly localized increase of stress is not directly measured by our (slightly) off-fault measurements, τ_p as well as the fracture energy Γ (the dissipated energy per unit area), were obtained independently (*2*, *3*) by analyzing the sub-Rayleigh crack propagation regime for this system. Briefly, Γ was extracted from the $1/\sqrt{r}$ LEFM singular form of the stresses, and τ_p was obtained from measurements of the cohesive zone size (details are provided in Materials and Methods). While inhomogeneities along the frictional interface are reflected in spatial variations of both and Γ and τ_p, we find that Γ and τ_p are independent of the rupture velocity. We therefore use these inferred values in analyzing the behavior of the system in the supershear regime.

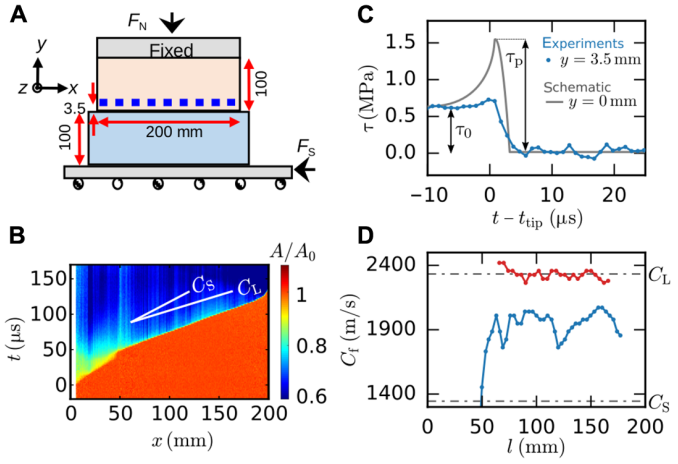

Fig. 1. Experimentally measured supershear rupture velocities. (**A**) Two PMMA blocks are used in a stick-slip friction experiment. We consider the elastic medium to be 2D with a quasi 1D frictional interface and measured the full 2D tensorial strains along and ≈3.5 mm above the frictional interface (blue squares). (**B**) Real contact area $A(x, t)$ measurements along the interface, normalized before the event, show rupture nucleation at $x \approx 0$, acceleration, and transition to supershear at $x \approx 50$ mm. (**C**) Shear stress variations, $\tau = \sigma_{xy} - \sigma^r_{xy}$, relative to the rupture tip arrival time, t_{tip}, measured at $x = 105$ mm. Arrows denote the dynamic stress drop τ_0 and peak shear strength τ_p. We obtain τ_p from the measured cohesive zone size. The gray curve schematically depicts the interfacial shear stress evolution. (**D**) Measured rupture velocities for two examples of rupture events in experiments with a dry interface. (B), (C), and the blue example in (D) correspond to the same rupture event.

The rupture front velocity $C_f(l)$, inferred from the measurements of $A(x, t)$ for the event presented in Fig. 1B, is shown in Fig. 1D (blue curve), along with an additional rupture event (red curve) whose high propagation speed approaches the longitudinal wave speed C_L. Here, l denotes the rupture length (as ruptures are nucleated at $x \approx 0$), and $C_f = \dot{l}$. What dictates $C_f(l)$ and how it relates to τ_0 and the frictional properties of the interface is the central question investigated in this article.

We now briefly describe how LEFM can be used to provide quantitative predictions for the speeds of supershear frictional rupture fronts. Within the wake of frictional ruptures, the bodies are always in partial contact [$\sigma_{yy}(x) \neq 0$], and the frictional resistance, σ^r_{xy}, opposes sliding. The problem of frictional rupture fronts, propagating within an interface separating identical materials, can be mapped to the stress-free conditions that define the mode II crack problem (*29*) by using the linearity of the governing equations and defining the shear stress variations, $\tau = \sigma_{xy} - \sigma^r_{xy}$ (see definition of τ, τ_0, and τ_p in Fig. 1C). The stress fields near the tip of an idealized supershear crack with no cohesive zone are singular (*26*, *30*, *31*), $\tau \sim K/(x - l)^g$, where K is the stress intensity factor and where, in contrast to sub-Rayleigh ruptures, the singular exponent g depends on C_f [with $g(C_f/C_L) \leq 1/2$]. K has been calculated explicitly only for a handful of particular examples, such as a semi-infinite crack subject to a pair of concentrated shear forces (*27*) or for a symmetric bilateral crack subject to uniform remote shear stress (*26*). In both cases, cracks were assumed to expand at constant velocity. A consequence of the singular description of supershear cracks is the vanishing energy flux into the crack tip for $C_f \neq \sqrt{2}C_S$. It was shown (*31*), however, that when a cohesive zone is introduced, a finite region where these singularities are regularized to a finite τ_p value, the requirement for a positive energy flux to the crack tip is fulfilled for any $C_f > C_S$. By combining the cohesive zone model with the constant-velocity singular crack solution, the energy flow to the crack tip per unit area (the energy release rate) G can be calculated (*26*–*28*). Here, we follow Broberg's bilateral crack solution (*26*), where G was expressed in terms of C_f, τ_0, l, and the cohesive zone size x_c. Here, motivated by recent experimental results (*2*), which showed that the interface shear strength τ_p is roughly independent of C_f (in contrast to the C_f dependence of x_c), we rederive G in terms of and C_f/C_L, l, τ_0, and τ_p. Balancing G and Γ yields a crack propagation criterion

$$\Gamma = G = \frac{\tau_p^2 l}{\mu}\left(\frac{\tau_0}{\tau_p}\right)^{1/g} \tilde{B}(C_f/C_L)\tilde{\Gamma}_D(g) \quad (1)$$

where μ is the shear modulus and $\tilde{B}(C_f/C_L)$ and $\tilde{\Gamma}_D(g)$ are known functions. The shape of the stress distribution within the cohesive zone is carried within $\tilde{\Gamma}_D(g)$ [see Materials and Methods for the derivation and definition of $\tilde{B}(C_f/C_L)$ and $\tilde{\Gamma}_D(g)$].

Studies of supershear crack arrest (*24*) showed that steady-state singular fields are not established instantaneously. Therefore, a solution of an accelerating crack cannot be constructed by the superposition of constant-velocity crack solutions, as had been performed previously for sub-Rayleigh propagation (*23*). In this sense, while Eq. 1 was strictly derived to describe cracks propagating at a constant velocity, we hypothesize that its applicability can be extended for "slowly" accelerating cracks, where velocity history can be neglected. As Eq. 1 implicitly links C_f to l, it will provide an equation of motion for supershear cracks.

The salient property of the supershear crack growth criterion (Eq. 1) is its dependence on the cohesive zone characteristics, in striking contrast to sub-Rayleigh brittle cracks (*9*, *30*). In addition, note the emergence of a characteristic length scale $l_0 = \frac{\mu\Gamma}{\tau_p^2}$, which is proportional to the static cohesive zone size. Finally, we note that the construction of Eq. 1 describes velocity response to spatial changes in interface properties [$\Gamma(x)$ and $\tau_p(x)$], as for sub-Rayleigh cracks. The rupture response to nonuniform spatial profiles, $\tau_0(x)$, is not captured by Eq. 1. We will consider this question in a later section of this article.

To investigate the applicability of the LEFM equation of motion, we supplement the experiments with two-dimensional (2D) numerical simulations of dynamic bilateral shear cracks using a spectral boundary integral method (*32*). The modeled system consists of two linear elastic semi-infinite half spaces with an interface governed by a linear slip weakening friction law (see Materials and Methods) and τ_0 applied along the interface. Poisson ratio $\nu = 0.35$ and plane strain are assumed ($C_S/C_L = 0.48$). We use a weak patch ($\tau_0/\tau_p = 0.8$) around the nucleation center to promote a direct transition (*20*) to supershear propagation. To test the predictions of Eq. 1 for various τ_0/τ_p values, we fix the value of τ_0/τ_p to 0.2 to 0.7 after a finite propagation distance (see Fig. 2A, top) by increasing τ_p and Γ (l_0 remains constant). This leads to an instantaneous response of the crack.

Figure 2 demonstrates that Eq. 1 provides an excellent description of both the numerical simulations and the experiments with no adjustable parameters. Lower τ_0 are associated with slower ruptures, as observed in early numerical work (*33*) and in sub-Rayleigh propagation (*3*). In our simulations, we observe transient discrepancies for the $\tau_0/\tau_p = 0.2$ case due to the strong localized increase of the interfacial strength ($l/l_0 = 140$ to 170). We expect these discrepancies when strong crack accelerations are present, as was previously discussed. We note that other types of transition to the supershear regime, for example, supershear seed crack or transition through a secondary crack, have been applied and result in equivalent observations (see Materials and

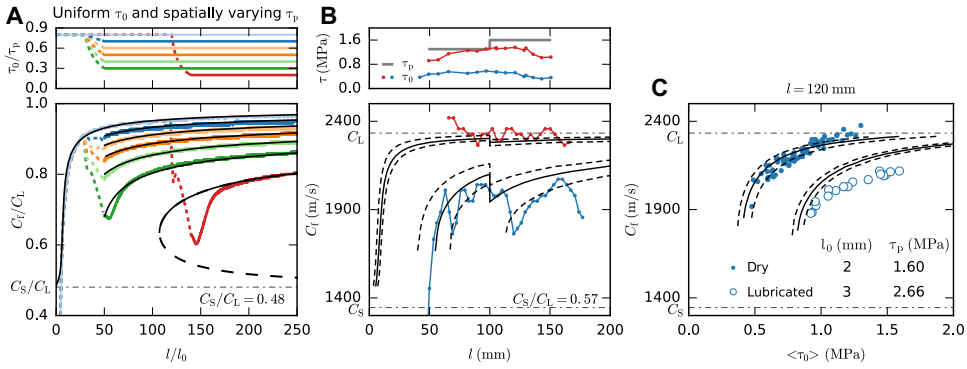

Fig. 2. Comparing theoretical predictions of supershear crack velocities with numerical simulations and experimental measurements. (**A**) Top: Spatially uniform τ_0 and nonuniform τ_p profiles are considered in simulations. The imposed τ_0/τ_p profiles are shown. Bottom: Colors represent the crack velocities $C_f(l)$ corresponding to the stress profiles in the top panel. τ_p is low, dashed lines, near the point of nucleation ($l/l_0 = 0$) and increases at distances 50 for $\tau_0/\tau_p > 0.2$ and at $l/l_0 = 130$ for $\tau_0/\tau_p = 0.2$ (red). Black solid lines denote predictions of Eq. 1. For sufficiently low τ_0/τ_p (red example), two solution branches to Eq. 1 exist (dashed line shows the unstable solution). (**B**) Top: Profiles of the measured shear stress τ_0 and estimated interfacial strength τ_p in experiments. Bottom: Measured rupture velocities for rupture events with stresses shown in the top panel. Theoretical predictions according to Eq. 1 are shown (solid lines); average τ_0 values are used, $l_0 = \mu\Gamma/\tau_p^2 = 2$ mm. Dashed lines correspond to the error estimates of l_0 and τ_p. (**C**) C_f, measured at $l = 120$ mm (averaged over ±10 mm), for multiple experiments is plotted with respect to the measured τ_0 profiles averaged over the same interval. Solid dots and open circles indicate experiments performed with dry and boundary-lubricated interfaces, respectively. Black lines are the theoretical predictions with the estimated errors.

Methods). In our experiments, rupture nucleation, acceleration, and the supershear transition are sensitive to the high stress gradients in the block edge vicinity and are beyond the scope of the current study. Instead, we concentrate on the sustained supershear propagation within a central region where these edge effects are negligible. Note the spatial variation of the τ_p obtained profile and the accompanying response of the equation of motion (Fig. 2B).

Figure 2C demonstrates the generality of the experimental results, where we consider both dry and boundary-lubricated interfaces, each with significantly different values of Γ and τ_p (*3*, *34*). Here, we compare the predictions of Eq. 1 at a fixed spatial position for multiple rupture events driven at different levels of τ_0/τ_p. Slight discrepancies for the boundary lubrication case might result from nonuniformity of τ_0 along the interface, which is not taken into account here.

In systems with uniform τ_0, τ_p, and Γ, the sub-Rayleigh–to–supershear transition [the Burridge-Andrews mechanism (*4*–*6*, *9*, *18*)] occurs only along weak interfaces above a critical value of τ_0/τ_p, and no supershear crack can exist for lower values of τ_0/τ_p. These critical values depend on C_S/C_L; $\tau_0/\tau_p = 0.31$ and 0.37 for $C_S/C_L = 0.48$ (simulations) and 0.57 (experiments), respectively. Both our simulations and experiments reveal strong hysteretic behavior; once a supershear crack has been excited [for example, the transition is facilitated through spatial nonuniformity (*17*, *19*, *35*)], supershear cracks may propagate in regions of strong interfaces, well below the critical τ_0/τ_p values given by the homogeneous Burridge-Andrews transition mechanism. For example, the green and red simulated examples (Fig. 2A) correspond to $\tau_0/\tau_p = 0.3$ and 0.2, respectively. Similarly, the particularly slow laboratory supershear rupture, $C_f \approx \sqrt{2}C_S$ (blue example in Fig. 2B), corresponds to $\tau_0/\tau_p < 0.37$, suggesting that, in this case, the transition has not been induced by the Burridge-Andrews mechanism but rather by favorable heterogeneities (*19*) at the block edge.

Minimal length for supershear propagation

The LEFM-based equation of motion describes two distinct shapes. For high prestress levels, for example, $\tau_0/\tau_p = 0.8$ (blue example in Fig. 2A), C_f monotonically increases with increasing l. As τ_0/τ_p is decreased, however, the solution bifurcates into two branches, for example, $\tau_0/\tau_p = 0.2$ (red example in Fig. 2A), one of which appears to be unstable (dashed line in Fig. 2A). The accelerating branch (the physical solution) only appears at a finite crack length l_m, predicting that no supershear cracks can exist for $l < l_m$. Thus, l_m represents a critical length for supershear propagation, similar to Griffith's length for the sub-Rayleigh regime (*31*). We have confirmed this prediction for several values of τ_0/τ_p by varying the length of the weak patch in our simulation (Fig. 3A). If the weak patch exceeds l_m, then the crack obeys the supershear equation of motion in the following stronger region. However, in cases where the weak patch ends at $l < l_m$, the crack transitions instantaneously to the sub-Rayleigh regime. From this point, the crack remains at the sub-Rayleigh regime even for $l > l_m$, where the supershear solutions exist. This demonstrates the coexistence of the sub-Rayleigh and supershear propagation solutions and the hysteretic transition between the two.

Figure 3B describes the dependence of l_m on τ_0. No critical length exists for sufficiently high stress levels. For $\tau_0/\tau_p \lesssim 0.45$, a finite value of l_m emerges and l_m increases rapidly with decreasing τ_0. We find empirically that $C_f(l_m) \approx \sqrt{2}C_S$; hence, by using Eq. 1, l_m can be approximated by

$$l_m \approx \frac{\mu\Gamma}{\tau_0^2} \cdot \frac{1}{\tilde{B}(\sqrt{2}C_S/C_L)} \qquad (2)$$

Figure 3B shows a comparison of Eq. 2 with the exact solution of Eq. 1. This approximation reveals that when it exists, the scale of l_m is determined by the Griffith length for crack nucleation $l_c \sim \mu\Gamma/\tau_0^2$ ($l_m \approx 3.7 l_c$ for $C_S/C_L = 0.48$). We emphasize that the minimal length presented here defines whether the supershear solution does or does not exist, which is fundamentally different from the question of what determines the sub-Rayleigh–to–supershear transition and whether it actually occurs (for example, Andrew's transition length, which is, in a uniform setup, always larger than l_m).

Supershear propagation along interfaces with nonuniform loading

Both changes in frictional strength (barriers) and nonuniform prestress (asperities) affect fault ruptures. These heterogeneities influence not only rupture propagation (*17*) but also produce different ground motions (*36*). In Fig. 4A, we show simulations that model nonuniform loading to illustrate the differences in the effect of barriers versus asperities for

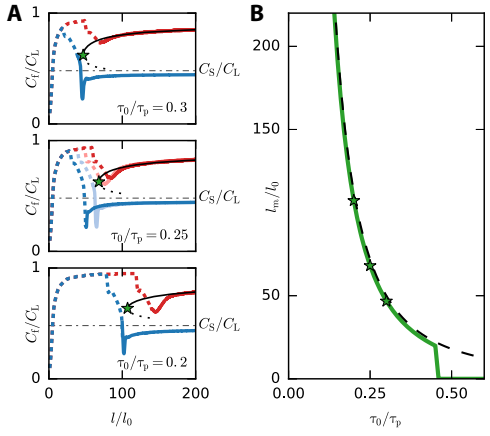

Fig. 3. Minimal lengths exist for supershear crack propagation under uniform loading. (**A**) Crack simulations for nonuniform τ_0/τ_p profiles (see Fig. 2A, top), where the size of the weak patch is varied. Dashed and solid curves indicate propagation within the weak and strong regions, respectively. τ_0/τ_p values in the figure correspond to the strong region (in the weak region, τ_0/τ_p = 0.8). Supershear propagation in the strong region cannot be sustained for $l < l_m$ (l_m is indicated by stars), where the supershear–to–sub-Rayleigh transition occurs. (**B**) l_m obtained numerically (green line) from Eq. 1 shows that no minimal length exists for $\tau_0/\tau_p \gtrsim 0.45$ (for fixed C_S/C_L). Normalization by l_0 and τ_p is applied for convenient comparison to (A). Stars correspond to the values denoted in (A). The dashed line is the analytic approximation based on Eq. 2.

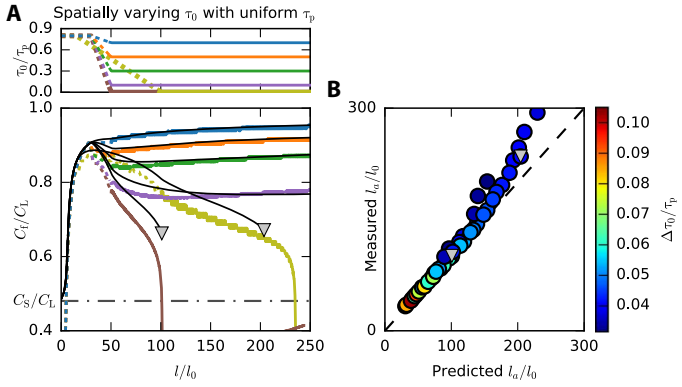

Fig. 4. Comparing theoretical predictions of supershear rupture velocities to numerical simulations for nonuniform prestress. (**A**) Top: Spatially nonuniform τ_0 profiles with uniform τ_p profiles are considered. The imposed τ_0/τ_p profiles are shown. Bottom: Rupture velocities $C_f(l)$ corresponding to the stress profiles in the top panel. Top and bottom: A high-stress nucleation patch (τ_0/τ_p = 0.8 region) facilitates a direct supershear transition. Black solid lines show theoretical predictions for the nonuniform loading described by Eq. 3. Note the difference of $C_f(l)$ profiles with those in Fig. 2A for similar τ_0/τ_p profiles. Predicted locations for supershear–to–sub-Rayleigh transition are marked by gray triangles. (**B**) Comparison of supershear–to–sub-Rayleigh transition positions measured in 50 simulations, with the predicted transition position based on Eq. 3. In the considered $\tau_0(x)$ profiles, the size of the high-stress nucleation patch is modified [see yellow curve in (A)]. Dashed line with slope 1 and is given for reference. Colors indicate the minimal needed increase in τ_0 within the low-stress region that would negate the predicted supershear–to–sub-Rayleigh transitions. Gray triangles denote the simulations shown in (A).

supershear propagation; changes in τ_0/τ_p are now induced by varying τ_0, in contrast to the simulations shown in Fig. 2A, where τ_0/τ_p profiles were varied by spatial changes in τ_p and Γ.

Note that in the context of LEFM, spatial variations in τ_0 are fundamentally different from those in τ_p (see Materials and Methods). Equation 1 assumed uniform prestress and cannot be strictly applied to nonuniform loading configurations. We therefore need to generalize Eq. 1 for spatially varying τ_0. To accomplish this, the information about the $\tau_0(x)$ profile should be incorporated within K. We assume $K = \kappa(C_f/C_L)K_s(\tau_0, l, g)$ and hypothesize that K_s is a weighted integral functional of $\tau_0(x)$ that can be calculated in a manner analogous to the static stress intensity factor used for sub-Rayleigh cracks (see Materials and Methods). This yields

$$\Gamma = G = \frac{\tau_p^2}{\mu}\left(\frac{K_s(\tau_0, l, g)}{\tau_p}\right)^{1/g}\tilde{B}(C_f/C_L)\tilde{\Gamma}_D(g) \qquad (3)$$

which coincides with Eq. 1 for uniform loading. Figure 4A shows predicted rupture speeds based on Eq. 3. Equation 3 generally compares well to simulations with minor discrepancies that appear in regions immediately following nonuniform areas. Note that even though the τ_0/τ_p profiles appear to be very similar to the nonuniform strength configurations in Fig. 2A, the dynamics are significantly different, reflecting the influence of the spatial variation of τ_0. For instance, while Eq. 2 predicts that at $\tau_0/\tau_p \approx 0.15$ no supershear cracks can exist for $l/l_0 < 200$ (see Fig. 3), Eq. 3 predicts sustained supershear propagation at τ_0/τ_p = 0.1 (see violet example in Fig. 4).

Only for extremely low background stress levels do we observe the transition to sub-Rayleigh propagation (see yellow and brown curves in Fig. 4A). At the crack length l_a of this transition, similar to the minimal supershear crack length l_m (Fig. 3), the energy flux to the crack tip is insufficient to drive supershear cracks. Figure 4B shows a systematic comparison between predicted supershear to sub-Rayleigh transitions and measured results from simulations for 50 different prestress configurations. To evaluate the criticality of prestress configurations, we computed the additional background stress $\Delta\tau_0$ required to prevent the transition to sub-Rayleigh (shown in color in Fig. 4B) and sustain supershear propagation. Simulations with lower prediction accuracy have lower $\Delta\tau_0$ and hence exhibit an extreme sensitivity to values of the prestress driving the transition. The prediction works generally well, although low values of $\Delta\tau_0/\tau_p$ result in underpredicted l_a for $l_a/l_0 > 180$. Thus, small changes in the background prestress, for instance due to wave radiation from the crack, which have been neglected in the current theoretical description, should have considerable effects on the rupture dynamics and could explain the prediction discrepancies.

DISCUSSION

Our measurements and simulations have shown that the energy balance at the rupture tip (Eqs. 1 and 3) provides quantitative predictions for the evolution of $C_f(l)$. These results are general so long as several necessary assumptions are satisfied. For instance, a region in the rupture tip's vicinity should exist where the stresses are singular $\tau \sim 1/(x - l)^g$. While typically this is assumed to be true when $l \gg x_c$, this condition is hard to meet for $\tau_0 \to \tau_p$, where $g \to 0$. Furthermore, in all rupture events considered here, shear waves that originate at the rupture nucleation (*9*, *18*) trail behind the supershear rupture tip. However, one might consider more complex scenarios. Rough faults, for example, may lead to rapid acceleration and deceleration of sub-Rayleigh ruptures (*35*) that would result in stress wave radiation. If the sub-Rayleigh–to–supershear transition were to occur at later times, then the supershear rupture will eventually catch up with these waves, and our assumption of time-independent loading will be violated. Finally, in our experiments, there

is no significant variation of σ^r_{xy} after the passage of the rupture tip (*37*), and frictional ruptures can be mapped to simple cracks with traction-free faces. Slip pulses (*15*, *38*), which may result because of strong velocity weakening of friction (*39*) and rapid healing of the interface, are fundamentally different from crack-like slip fronts and would require a different predictive theoretical model.

Natural faults are complex entities that include significant heterogeneity of fracture energy, friction laws, and stresses. Furthermore, complicated fault geometry, together with significant challenges in measuring the speeds of supershear earthquakes (*11*, *12*, *14*) and determining fault properties, often hinder comparisons with modeling. In some cases, qualitative and sometimes quantitative features of natural earthquakes can be successfully compared with idealized numerical models (*13*) and laboratory experiments (*40*). This fracture mechanics–based picture presented in this article is one of these, as it provides new and significant fundamental understanding of supershear rupture dynamics. These ideas may be potentially generalized to further account for the complexities associated with natural earthquakes.

Our results not only highlight how key parameters such as τ_0, τ_p, and Γ control supershear earthquakes but also provide a tool for quantitative predictions of supershear rupture speeds. These results have important implications, as the propagation speeds of supershear earthquakes dictate the amplitudes of the stress fields along the radiated Mach fronts (*15*). These amplitudes, while disappearing at $C_f = \sqrt{2}C_S$, greatly increase as $C_f \rightarrow C_L$. These subtle changes of the supershear earthquake speeds, therefore, have significant impact on off-fault damage and provide a key parameter for predicting the serious seismic hazards that these earthquakes impose.

Finally, while supershear earthquakes are typically associated with highly stressed faults, our results support suggestions (*19*) that supershear earthquakes may exist even at extremely low stress levels, if favorable heterogeneities for supershear transition are present. The proposed equation of motion provides exact conditions for which these low stress earthquakes may or may not sustain supershear propagation and can explain supershear–to–sub-Rayleigh transitions such as those in (*19*). This work, furthermore, provides fundamental insights for understanding how the crucial interplay between fault roughness and stress levels (*35*) may govern supershear rupture.

MATERIALS AND METHODS

Experimental system

Our experiments were conducted using PMMA plates ($\rho \approx 1170$ kg/m^3) of dimensions 200 mm × 100 mm × 5.5 mm (top block) and 240 mm × 100 mm × 5.5 mm (bottom block) in the x, y, and z directions, respectively (see Fig. 1A). The blocks were pressed together by applying ≈5 MPa of nominal pressure. The contacting surfaces were cleaned with distilled water and isopropyl alcohol and then dried for about 2 hours (termed here dry interfaces). We also conducted experiments in the boundary-lubrication regime (*3*, *34*), where contacting surfaces were coated by a thin layer of lubricant (silicon oil with kinematic viscosity $\nu \approx 100$ mm^2/s). Material shear, C_S, and longitudinal, C_L, wave speeds were obtained by measuring the time of flight of ultrasonic pulses, yielding $C_S = 1345 \pm 10$ m/s and $C_L = 2700 \pm 10$ m/s, corresponding to the plane strain hypothesis ($\varepsilon_{zz} = 0$). Using these measured values, we calculated that for plane stress conditions ($\sigma_{zz} = 0$), $C_L \approx 2333$ m/s ($C_S/C_L \approx 0.58$) and $C_R \approx 1237$ m/s. The corresponding dynamic shear modulus is $\mu = 2.1$ GPa (*9*). The three components of the 2D strain tensor were continuously and simultaneously measured by Vishay 015RJ rosette strain gages every 1 μs at 16 to 19 spatial locations, ~3.5 mm above the frictional interface (*2*).

In previous work (*2*), it was found that the strains in the vicinity of rupture tips, propagating below C_R, are well described by the square-root singular LEFM solutions, originally derived to describe brittle shear cracks. This comparison of the solutions with the measured strains provides a measure of the fracture energy Γ, which was found to be roughly independent of rate. Furthermore, it was suggested that measurements of the contact area A variations provide a direct measurement of the cohesive zone size, x_c (*2*). The theoretical interface strength τ_p is defined as the difference between the actual interface strength and the residual stress σ^r_{xy} (see Fig. 1C). τ_p is obtained from measured values of Γ and x_c using the simplest cohesive zone models (*29*, *41*). For the current set of experiments, we measured slight spatial inhomogeneities of the frictional interface. In the dry case, for 50 mm < x < 100 mm, $\Gamma \approx 1.5$ J/m^2 and $\tau_p \approx 1.3$ MPa, while for 100 mm < x < 150 mm, $\Gamma \approx 2.5$ J/m^2 and $\tau_p \approx 1.6$ MPa. This effective step increase of Γ was used to compare our measurements to the predictions of Eq. 1 in Fig. 2B. In the boundary-lubrication regime, for 100 mm < x < 150 mm, $\Gamma \approx 10$ J/m^2 and $\tau_p \approx 2.66$ MPa. Details can be found in the Supplemental Material of (*3*). In general, the measured values of Γ and τ_p obtained for the sub-Rayleigh regime were used here for supershear ruptures.

Numerical simulations

Our numerical results were generated by solving elastodynamic equations with the spectral boundary integral method (*32*, *42*). The propagation of a dynamic crack between two half spaces was modeled with a cohesive-type approach to describe the tractions along the weak interface. An explicit time integration was applied. The spectral formulation of the tractions and displacements at the interface results in a periodic setup. In our simulations, we used a replication length of 1.2 m with a discretization of 8192 nodes. The half-space material is linear elastic. To compare with the experiments, we applied a dynamic value of the elastic modulus $E = 5.65$ GPa, Poisson's ratios $\nu = 0.35$, and density $\rho = 1170$ kg/m^3 and used a plane strain assumption ($C_S/C_L \approx 0.48$). The interface tractions were governed by a linear slip-weakening cohesive law, $\tau(\delta) = \tau_p(1 - \delta/d_c)$ for $0 < \delta < d_c$, which imposes a strength that decreases linearly with slip δ from a peak value τ_p to zero over a characteristic slip weakening distance d_c. Reference values applied in the uniform setup were $\tau_p = 1.0$ MPa and $d_c = 2$ μm, which led to a fracture energy of $\Gamma = 1.0$ J/m^2. Rupture nucleation was triggered via slowly propagating a seed crack of imposed velocity $0.1C_R$ [following (*9*)] through the nucleation zone. In the nucleation zone, the value of τ_p was gradually reduced to zero (over a length of ≈6 mm). Once the seed crack reached a critical distance l_c (the Griffith length), rupture acceleration initiated and the ruptures propagated dynamically.

While $\nu = 0.35$ occurs in serpentinized mantle material (*43*) as, for instance, along the Denali fault (*44*) that hosted a supershear earthquake (*12*, *13*, *45*), $\nu = 0.25$ is a common value for granite. Additional numerical results were obtained with $\nu = 0.25$ and plane strain boundary conditions ($C_S/C_L = 0.577$). Comparisons with the theoretical predictions are shown in fig. S1. The results are qualitatively identical to Fig. 2. The main quantitative difference is that the ruptures accelerate over shorter distances to considerably higher speeds, that is, $C_f/C_L > 0.9$. Therefore, the differences in rupture speed for very different prestress levels are already relatively small shortly after transition.

Here, we used spatially nonuniform τ_0/τ_p profiles. Direct supershear transition was triggered by using high τ_0/τ_p levels for very short crack

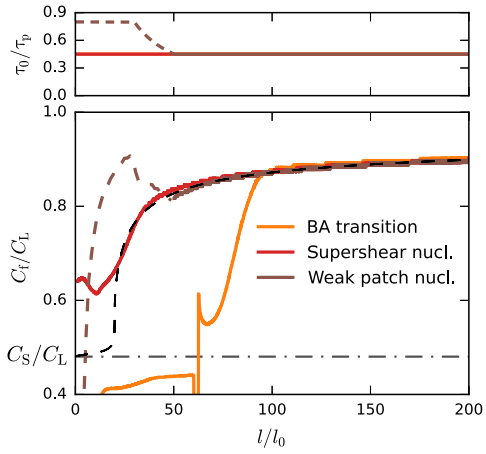

Fig. 5. The effect of sub-Rayleigh–to–supershear transition on the equation of motion of supershear cracks. Three different transition mechanisms are considered. Top: The first setup (brown curve) has a spatially nonuniform τ_0/τ_p profile with reduced local τ_p for $l/l_0 < 50$ (see main text for details). Two additional examples have spatially uniform τ_0/τ_p profiles (orange and red curves). Bottom: Colors represent the crack velocities $C_f(l)$ corresponding to the stress profiles in the top panel. Brown curve indicates continuous crack acceleration to supershear speeds (direct transition) within a weakened nucleation (nucl.) patch (high τ_0/τ_p level). Orange curve indicates sub-Rayleigh rupture transitions at $l/l_0 \approx 65$ to supershear speed through the Burridge-Andrews (BA) mechanism (*4*, *5*). Red curve indicates an imposed supershear seed crack leads to a self-sustained supershear crack propagation. The black dashed line denotes theoretical prediction for a spatially uniform prestress level ($\tau_0/\tau_p = 0.45$).

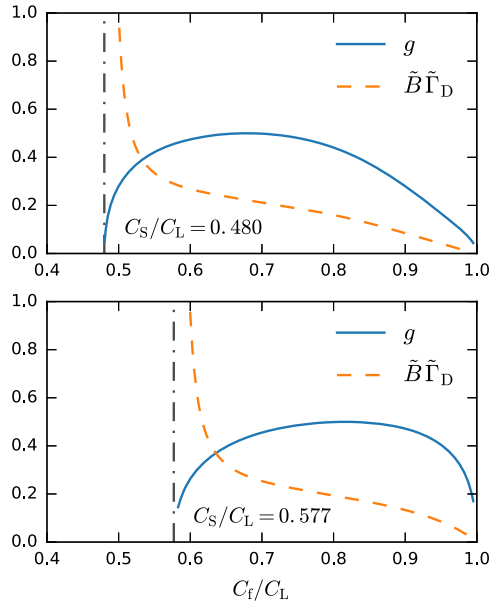

Fig. 6. Calculated $g(\beta)$ and $\tilde{B}(C_f/C_L)\tilde{\Gamma}_D(g)$. $g(\beta)$ and the product of $\tilde{B}(C_f/C_L)$ and $\tilde{\Gamma}_D(g)$, as appearing in Eq. 1, are provided for $C_S/C_L = 0.48$ (top) and $C_S/C_L = 0.577$ (bottom). $\tilde{\Gamma}_D(g)$ was calculated assuming a linear cohesive zone model.

lengths. Supershear propagation was then studied as cracks entered into regions with lower values of τ_0/τ_p (for example, brown curve in Fig. 5). We have also tested the quality of the theoretical prediction for supershear ruptures after transition through the well-known Burridge-Andrews mechanisms (orange curve in Fig. 5). The rupture first propagates in the sub-Rayleigh regime until a radiated shear wave ahead of the crack tip nucleates a secondary crack that then propagates at supershear speeds. A third simulated rupture was initiated by a seed crack that propagated at supershear speeds already during the nucleation procedure. All three tested supershear transition mechanisms lead to supershear ruptures with propagation speeds that are, after brief transient differences, quantitatively well described by our theoretical model. The observed discrepancies within this transient period, we believe, are related to the history dependence, discussed by Huang and Gao (*24*), which was neglected in the derivation of Eq. 1.

Theoretical framework

In what follows, we briefly describe how LEFM can be used to provide quantitative predictions for supershear rupture propagation following Broberg (*26*). The self-similar solution (*26*, *31*) for a symmetrical bilateral singular crack expanding at a constant speed under uniform remote shear stress τ_0 provides

$$\tau \to \kappa(C_f/C_L)\tau_0\left(\frac{l}{x-l}\right)^g \text{ as } x \to l^+ \tag{4}$$

where l is the crack half length and $\kappa(C_f/C_L)$ a known function.

A nonrealistic consequence of the singular description is the vanishing energy flux into the crack tip for $C_f \neq \sqrt{2}C_S$. It was shown (*31*), however, that when a cohesive zone is introduced, a finite region where these singularities are regularized, the requirement for a positive energy flux to the crack tip is fulfilled for any $C_f > C_S$. The energy flux is given by

$$G = \frac{\tau_p^2 x_c}{\mu}\tilde{G}(C_f/C_L) \tag{5}$$

Here, μ is the shear modulus, τ_p (the peak shear strength) is defined in Fig. 1, x_c is the cohesive zone size, and $\tilde{G}(C_f/C_L)$ is a known function containing information about the shape of the stress distribution within the cohesive zone. Furthermore, as small-scale yielding is assumed (that is, $l \gg x_c$ and $\tau_p \gg \tau_0$), the shear stress of these cohesive zone models recovers the singular form at large distances from the crack tip (*31*)

$$\tau \to \kappa_c(g)\tau_p\left(\frac{x_c}{x-l}\right)^g \text{ for } x - l \gg x_c \tag{6}$$

where $\kappa_c(g)$ is another known function. The complete form of Eqs. 4, 5, and 6 are given, respectively, by Eqs. 52, 66, and 64 in (*26*), with slight changes in the notations: τ_p, x_c, τ_0, and g denote τ_D, d, τ_{xy}^{∞}, and γ.

G can be expressed in terms of τ_0 and l, by comparing the two independent forms for τ (Eqs. 4 and 6). This intermediate asymptotic matching was also used by Huang and Gao (*24*) and Antipov *et al.* (*28*). In (*26*), G was determined as a function of C_f/C_L, l, τ_0, and x_c [Eq. 68 in (*26*)] and given by

$$G = \frac{\pi\tau_0^2 l}{\mu}\left(\frac{x_c}{l}\right)^{1-2g} B(C_f/C_L)\Gamma_D(g) \tag{7}$$

where $B(C_f/C_L)$ and $\Gamma_D(g)$ are known functions where the shape of the stress distribution within the cohesive zone is contained within $\Gamma_D(g)$. Here, motivated by recent experimental results (*2*), which showed that τ_p is roughly independent of C_f (in contrast to the C_f dependence of x_c), we rederived G in terms of C_f/C_L, l, τ_0, and τ_p

$$G = \frac{\tau_p^2 l}{\mu}\left(\frac{\tau_0}{\tau_p}\right)^{1/g}\tilde{B}(C_f/C_L)\tilde{\Gamma}_D(g) \quad (8)$$

$\tilde{B}(C_f/C_L)$ and $\tilde{\Gamma}_D(g)$ are given by

$$\tilde{B}(C_f/C_L) = \left(\frac{\pi C_f/C_L e^{-I_0}}{2^{1-g}gN}\right)^{1/g}\frac{f_1\sin(\pi g)}{\pi}\left(\frac{1-C_f/C_L}{1+C_f/C_L}\right) \quad (9)$$

$$\tilde{\Gamma}_D(g) = 2\left(\int_0^\infty \frac{D(-\omega)}{\omega^{1-g}}d\omega\right)^{-1/g}\omega_D(g) \quad (10)$$

where I_0, N, f_1, and ω_D are given explicitly in (*26*) and can be calculated once C_f/C_L and C_S/C_L are specified. Note that the cohesive zone properties are only contained within $\tilde{\Gamma}_D(g)$. $D(\omega)$ defines the shape of the stress distribution within the cohesive zone; for $\xi = x - x_{tip} < 0$, the shear stress gradually decreases according to a prescribed shear stress profile, $\tau(\xi) = \tau_p D(\xi/x_c)$. We chose $D(\xi/x_c) = e^{\xi/x_c}$ to describe the experimental results. Our numerical simulations use a more simply implemented linear slip-weakening cohesive law $\tau(\delta)$ (see "Numerical simulations" section). For simplicity, we modeled simulated ruptures by a linear spatial stress distribution within the cohesive zone through $D(\xi/x_c) = 1 + \xi/x_c$ for $-1 < \xi/x_c < 0$. Although some deviations between the models exist [for example, linear spatial profiles of $D(\xi)$ result in nonlinear slip laws $\tau(\delta)$, see Fig. 16 in (*15*)], we explicitly verified that these deviations have negligible effects on the resulting equation of motion.

Figure 6 shows $g(C_f/C_L)$ and the product of $\tilde{B}(C_f/C_L)$ and $\tilde{\Gamma}_D(g)$ [$\tilde{\Gamma}_D(g)$ was calculated for a linear cohesive zone profile], so that the predictions of the supershear equation of motion (Eq. 1 in the main text) can be easily reproduced. At $C_f = \sqrt{2}C_S$, the singularity exponent $g = 1/2$ and $\Gamma_D(1/2) = \tilde{\Gamma}_D(1/2) = 1$. Therefore, Eqs. 7 and 8 coincide, and $G(\sqrt{2}C_S/C_L)$ is independent of the cohesive zone characteristics. Using these observations and explicitly verifying that $C_f(l_m) \approx \sqrt{2}C_S$, the approximated form for a critical length for supershear propagation, l_m, given by Eq. 2 in the main text, is easily obtained.

A crucial difference between Eqs. 4 and 6 exists. While Eq. 6 adapts rather quickly to spatial changes of interface properties, Eq. 4 (and therefore Eq. 1) does not account for nonuniform τ_0 due to the underlying assumption of the solution. In what follows, we consider supershear propagation along interfaces with nonuniform spatial profiles of $\tau_0(x)$.

We assume for supershear cracks the condition of small-scale yielding, $\tau \sim K/(x - l)^g$, where K is the stress intensity factor. The value of K explicitly incorporates the information about the $\tau_0(x)$ profile. The fundamental solution for semi-infinite supershear cracks propagating at a constant speed and subjected to a pair of suddenly applied concentrated shear forces is given by Eq. 30 in (*27*)

$$\tau \to \tilde{\kappa}(C_f/C_L)\frac{\tau^*}{l^{1-g}}\cdot\frac{1}{(x-l)^g} \text{ as } x \to l^+ \quad (11)$$

For a general $\tau_0(x)$ profile, $K = \tilde{\kappa}(C_f/C_L)K_s$ is obtained by integrating the fundamental solution following Freund's superposition method (*30*), which results in

$$K_s(l,g) = \int_0^l \frac{\tau_0(s)}{(l-s)^{1-g}}ds \quad (12)$$

Note the analogy with semi-infinite sub-Rayleigh cracks, where $K_s(l) \sim \int_0^l \frac{\tau_0(s)}{(l-s)^{1/2}}ds$.

As far as we know, an explicit solution analogous to Eq. 12 (which was derived for semi-infinite cracks) for propagating supershear bilateral cracks in our simulations has not been formulated. Therefore, we suggest that the sub-Rayleigh static stress intensity factor $K_s(l) \sim \int_0^l \tau_0(s)\left(\frac{l}{l^2-s^2}\right)^{1/2}ds$ can be extended to supershear propagation by

$$K_s(l,g) = \frac{1}{\tilde{K}_s(g)}\int_0^l \tau_0(s)\left(\frac{l}{l^2-s^2}\right)^{1-g}ds \quad (13)$$

The normalization factor $\tilde{K}_s(g) = \int_0^1 \left(\frac{1}{1-s^2}\right)^{1/g}ds$ ensures that the generalized form of the shear stresses given by

$$\tau \to \kappa(C_f/C_L, g)K_s(l,g)\frac{1}{(x-l)^g} \text{ as } x \to l^+ \quad (14)$$

recovers Eq. 4 for spatially uniform $\tau_0(x)$ profiles.

It is worth emphasizing again that Eqs. 11 and 12 are derived for cracks propagating at a constant speed. Previous work (*24*) has shown that a rigorous solution for accelerating cracks cannot be constructed by the superposition of these constant-velocity solutions, as had been performed previously for sub-Rayleigh propagation (*23*). In this sense, we hypothesized that these equations can be applied to problems with slowly varying crack speed. As the kernel in Eqs. 12 and 14 is singular, we assumed that the main contribution to the integral comes from the region $s \approx l$. Therefore, assuming that C_f varies slowly, we calculated the integral with a value of $g(C_f)$ that corresponds to the local crack speed at the crack position l. Finally, $C_f(l)$ is determined numerically by Eq. 3: For any crack length l, C_f is evaluated so that Eq. 3 is satisfied. Although this is in no way a rigorous derivation and some of the approximations here are uncontrolled, our conjecture is in good agreement with the simulations and provides a useful tool for describing supershear cracks subjected to nonuniform loading.

SUPPLEMENTARY MATERIALS

Supplementary material for this article is available at http://advances.sciencemag.org/cgi/content/full/4/7/eaat5622/DC1

Fig. S1. Comparison of theoretical predictions of supershear crack velocities with numerical simulations for various shear strength levels for $\nu = 0.25$ (plain strain).

REFERENCES AND NOTES

1. S. M. Rubinstein, G. Cohen, J. Fineberg, Detachment fronts and the onset of dynamic friction. *Nature* **430**, 1005–1009 (2004).
2. I. Svetlizky, J. Fineberg, Classical shear cracks drive the onset of dry frictional motion. *Nature* **509**, 205–208 (2014).
3. I. Svetlizky, D. S. Kammer, E. Bayart, G. Cohen, J. Fineberg, Brittle fracture theory predicts the equation of motion of frictional rupture fronts. *Phys. Rev. Lett.* **118**, 125501 (2017).

4. R. Burridge, Admissible speeds for plane-strain self-similar shear cracks with friction but lacking cohesion. *Geophys. J. Int.* **35**, 439–455 (1973).
5. D. J. Andrews, Rupture velocity of plane strain shear cracks. *J. Geophys. Res.* **81**, 5679–5687 (1976).
6. K. Xia, A. J. Rosakis, H. Kanamori, Laboratory earthquakes: The sub-Rayleigh-to-supershear rupture transition. *Science* **303**, 1859–1861 (2004).
7. O. Ben-David, G. Cohen, J. Fineberg, The dynamics of the onset of frictional slip. *Science* **330**, 211 (2010).
8. F. X. Passelègue, A. Schubnel, S. Nielsen, H. S. Bhat, R. Madariaga, From sub-Rayleigh to supershear ruptures during stick-slip experiments on crustal rocks. *Science* **340**, 1208–1211 (2013).
9. I. Svetlizky, D. Pino Muñoz, M. Radiguet, D. S. Kammer, J.-F. Molinari, J. Fineberg, Properties of the shear stress peak radiated ahead of rapidly accelerating rupture fronts that mediate frictional slip. *Proc. Natl. Acad. Sci. U.S.A.* **113**, 542–547 (2016).
10. S. Xu, E. Fukuyama, F. Yamashita, K. Mizoguchi, S. Takizawa, H. Kawakata, Strain rate effect on fault slip and rupture evolution: Insight from meter-scale rock friction experiments. *Tectonophysics* **733**, 209–231 (2017).
11. M. Bouchon, M. Vallée, Observation of long supershear rupture during the magnitude 8.1 Kunlunshan earthquake. *Science* **301**, 824–826 (2003).
12. K. T. Walker, P. M. Shearer, Illuminating the near-sonic rupture velocities of the intracontinental Kokoxili M-w 7.8 and Denali fault M-w 7.9 strike-slip earthquakes with global P wave back projection imaging. *J. Geophys. Res.* **114**, B02304 (2009).
13. E. M. Dunham, R. J. Archuleta, Evidence for a supershear transient during the 2002 Denali fault earthquake. *Bull. Seismol. Soc. Am.* **94**, S256–S268 (2004).
14. D. Wang, J. Mori, K. Koketsu, Fast rupture propagation for large strike-slip earthquakes. *Earth Planet. Sci. Lett.* **440**, 115–126 (2016).
15. H. S. Bhat, R. Dmowska, G. C. P. King, Y. Klinger, J. R. Rice, Off-fault damage patterns due to supershear ruptures with application to the 2001 M_w 8.1 Kokoxili (Kunlun) Tibet earthquake. *J. Geophys. Res.* **112**, B0631 (2007).
16. D. J. Andrews, Ground motion hazard from supershear rupture. *Tectonophysics* **493**, 216–221 (2010).
17. E. M. Dunham, P. Favreau, J. M. Carlson, A supershear transition mechanism for cracks. *Science* **299**, 1557–1559 (2003).
18. E. M. Dunham, Conditions governing the occurrence of supershear ruptures under slip-weakening friction. *J. Geophys. Res. Solid Earth* **112**, B07302 (2007).
19. Y. Liu, N. Lapusta, Transition of mode II cracks from sub-Rayleigh to intersonic speeds in the presence of favorable heterogeneity. *J. Mech. Phys. Solids* **56**, 25–50 (2008).
20. C. Liu, A. Bizzarri, S. Das, Progression of spontaneous in-plane shear faults from sub-Rayleigh to compressional wave rupture speeds. *J. Geophys. Res. Solid Earth* **119**, 8331–8345 (2014).
21. D. S. Kammer, D. Pino Muñoz, J. F. Molinari, Length scale of interface heterogeneities selects propagation mechanism of frictional slip fronts. *J. Mech. Phys. Solids* **88**, 23–34 (2016).
22. G. Albertini, D. S. Kammer, Off-fault heterogeneities promote supershear transition of dynamic mode II cracks. *J. Geophys. Res. Solid Earth* **122**, 6625–6641 (2017).
23. L. B. Freund, Crack propagation in an elastic solid subjected to general loading—II. Non-uniform rate of extension. *J. Mech. Phys. Solids* **20**, 141–152 (1972).
24. Y. Huang, H. Gao, Intersonic crack propagation—Part II: Suddenly stopping crack. *J. Appl. Mech.* **69**, 76–80 (2002).
25. G. Guo, W. Yang, Y. Huang, A. J. Rosakis, Sudden deceleration or acceleration of an intersonic shear crack. *J. Mech. Phys. Solids* **51**, 311–331 (2003).
26. K. B. Broberg, Intersonic bilateral slip. *Geophys. J. Int.* **119**, 706–714 (1994).
27. Y. Huang, H. Gao, Intersonic crack propagation—Part I: The fundamental solution. *J. Appl. Mech.* **68**, 169–175 (2001).
28. Y. A. Antipov, O. Obrezanova, J. R. Willis, A fracture criterion of "Barenblatt" type for an intersonic shear crack. *Math. Mech. Solids* **9**, 271–283 (2004).
29. A. C. Palmer, J. R. Rice, The growth of slip surfaces in the progressive failure of over-consolidated clay. *Proc. R. Soc. Lond. A Math. Phys. Sci.* **332**, 527–548 (1973).
30. L. B. Freund, The mechanics of dynamic shear crack propagation. *J. Geophys. Res. Solid Earth* **84**, 2199–2209 (1979).
31. K. B. Broberg, *Cracks and Fracture* (Academic, 1999).
32. P. H. Geubelle, J. R. Rice, A spectral method for three-dimensional elastodynamic fracture problems. *J. Mech. Phys. Solids* **43**, 1791–1824 (1995).
33. S. M. Day, Three-dimensional simulation of spontaneous rupture: The effect of nonuniform prestress. *Bull. Seismol. Soc. Am.* **72**, 1881–1902 (1982).
34. E. Bayart, I. Svetlizky, J. Fineberg, Slippery but tough: The rapid fracture of lubricated frictional interfaces. *Phys. Rev. Lett.* **116**, 194301 (2016).
35. L. Bruhat, Z. Fang, E. M. Dunham, Rupture complexity and the supershear transition on rough faults. *J. Geophys. Res. Solid Earth* **121**, 210–224 (2016).
36. M. T. Page, E. M. Dunham, J. M. Carlson, Distinguishing barriers and asperities in near-source ground motion. *J. Geophys. Res. Solid Earth* **110**, B11302 (2005).
37. I. Svetlizky, E. Bayart, G. Cohen, J. Fineberg, Frictional resistance within the wake of frictional rupture fronts. *Phys. Rev. Lett.* **118**, 234301 (2017).
38. E. M. Dunham, R. J. Archuleta, Near-source ground motion from steady state dynamic rupture pulses. *Geophys. Res. Lett.* **32**, L03302 (2005).
39. V. Rubino, A. J. Rosakis, N. Lapusta, Understanding dynamic friction through spontaneously evolving laboratory earthquakes. *Nat. Commun.* **8**, 15991 (2017).
40. M. Mello, H. S. Bhat, A. J. Rosakis, H. Kanamori, Reproducing the supershear portion of the 2002 Denali earthquake rupture in laboratory. *Earth Planet. Sci. Lett.* **387**, 89–96 (2014).
41. O. Samudrala, Y. Huang, A. J. Rosakis, Subsonic and intersonic shear rupture of weak planes with a velocity weakening cohesive zone. *J. Geophys. Res. Solid Earth* **107**, 2170 (2002).
42. M. S. Breitenfeld, P. H. Geubelle, Numerical analysis of dynamic debonding under 2d in-plane and 3d loading. *Int. J. Fracture* **93**, 13–38 (1998).
43. N. Hilairet, B. Reynard, Y. Wang, I. Daniel, S. Merkel, N. Nishiyama, S. Petitgirard, High-pressure creep of serpentine, interseismic deformation, and initiation of subduction. *Science* **318**, 1910–1913 (2007).
44. G. Rossi, G. A. Abers, S. Rondenay, D. H. Christensen, Unusual mantle poisson's ratio, subduction, and crustal structure in central Alaska. *J. Geophys. Res. Solid Earth* **111**, B09311 (2006).
45. D. Eberhart-Phillips, P. J. Haeussler, J. T. Freymueller, A. D. Frankel, C. M. Rubin, P. Craw, N. A. Ratchkovski, G. Anderson, G. A. Carver, A. J. Crone, T. E. Dawson, H. Fletcher, R. Hansen, E. L. Harp, R. A. Harris, D. P. Hill, S. Hreinsdóttir, R. W. Jibson, L. M. Jones, R. Kayen, D. K. Keefer, C. F. Larsen, S. C. Moran, S. F. Personius, G. Plafker, B. Sherrod, K. Sieh, N. Sitar, W. K. Wallace, The 2002 Denali fault earthquake, Alaska: A large magnitude, slip-partitioned event. *Science* **300**, 1113–1118 (2003).

Acknowledgments: We thank M. Adda-Bedia for fruitful discussions and his help. **Funding:** We also acknowledge the support of both the US-Israel Binational Science Foundation (grant no. 2016950) and Israel Science Foundation (grant no. 1523/15). **Author contributions:** D.S.K. performed the numerical work. I.S. performed the experimental and theoretical work. All authors contributed to the analysis and writing of the manuscript. **Competing interests:** The authors declare that they have no competing interests. **Data and materials availability:** All data needed to evaluate the conclusions in the paper are present in the paper and/or the Supplementary Materials. The computer code used for simulations, as well as the additional data related to this paper, may be requested from the authors.

Submitted 12 March 2018
Accepted 5 June 2018
Published 18 July 2018
10.1126/sciadv.aat5622

Citation: D. S. Kammer, I. Svetlizky, G. Cohen, J. Fineberg, The equation of motion for supershear frictional rupture fronts. *Sci. Adv.* **4**, eaat5622 (2018).

Science Advances

The equation of motion for supershear frictional rupture fronts

David S. Kammer, Ilya Svetlizky, Gil Cohen and Jay Fineberg

Sci Adv **4** (7), eaat5622.
DOI: 10.1126/sciadv.aat5622